Inorganic Chemistry

Article

pubs.acs.org/IC

# Incorporation of Thorium in the Zircon Structure Type through the $Th_{1-x}Er_x(SiO_4)_{1-x}(PO_4)_x$ Thorite−Xenotime Solid Solution

Adel Mesbah,*[,†] Nicolas Clavier,[†] M. Janeth Lozano-Rodriguez,[‡] Stephanie Szenknect,[†] and Nicolas Dacheux[†]

[†]ICSM, UMR 5257 CEA/CNRS/ENSCM/University of Montpellier, Site de Marcoule—Bât. 426, BP 17171, 30207 Bagnols-sur-Cèze cedex, France

[‡]HZDR, Institute of Resource Ecology, The Rossendorf Beamline at ESRF, P.O. Box 220, 38043 Grenoble, France

**ABSTRACT:** Pure powdered compounds with a general formula $Th_{1-x}Er_x(SiO_4)_{1-x}(PO_4)_x$ belonging to the zircon−xenotime family were successfully synthesized under hydrothermal conditions (250 °C, 7 days) as recently reported for the preparation of coffinite. Therefore, a thorough, combined PXRD, EDX, EXAFS, Raman, and FTIR analysis showed the formation of a solid solution in agreement with Vegard's law. Moreover, the examination of the local structure shows that the Th−O distances remain close to those found in $ThSiO_4$, whereas the Er−O distances show a significant decrease from 2.38(14) to 2.34(7) Å when increasing the erbium content from $x = 0.2$ to $x = 1$. The variation of the local structure also affects the $PO_4^{3-}$ groups that are surely distorted in the structure.

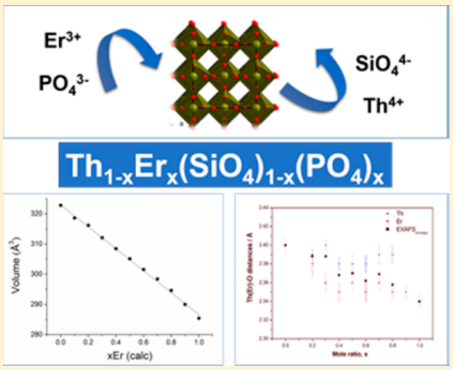


## 1. INTRODUCTION

The crystal chemistry of lanthanides phosphates ($Ln^{III}PO_4$) and actinides silicates ($An^{IV}SiO_4$) is governed, at high temperature, by the existence of two distinct structural types. On one hand, the monazite structure (monoclinic, space group $P2_1/n$)[1] is generally the most stable phase for light rare earth element (REE) phosphates (typically from La to Gd) and was also reported for $ThSiO_4$ (corresponding to the mineral huttonite)[2,3] and for $PaSiO_4$.[4] The original $MO_9$ coordination polyhedron encountered in the monazite confers to the structure the capability to incorporate a wide range of elements through direct and/or coupled substitutions, either on the cationic or the anionic site,[5] leading to a tremendous variety of applications. On the other hand, heavy REE phosphates (namely from $TbPO_4$ to $LuPO_4$) which relate to the mineral xenotime, and all tetravalent actinides phosphates (including $ThSiO_4$ thorite,[6] $USiO_4$ coffinite,[7,8] and associated solid solutions[9−12]), preferentially adopt the zircon-type structure in the tetragonal system with $I4_1/amd$ as a space group. Silicate-based compounds of this family then also include zircon ($ZrSiO_4$) and hafnon ($HfSiO_4$).

Monazite, xenotime, and zircon are widespread naturally occurring minerals.[13−18] They coexist in many granitic and metamorphic rocks located in different sites on earth[19−23] and exhibit a very rich structural diversity owing to their ability to contain a wide variety of rare earth elements (REEs) and natural actinides (U and Th). Indeed, these three minerals represent the main sources of the REE, U and Th on earth, with monazite being considered as the first source of thorium and coffinite as the second source of tetravalent uranium after uraninite.[13] Many works already demonstrated the utility of the presence of the actinides and associated daughter products (U−Th−Pb) for the precise dating of the rocks in the field of geochronology.[24−32] Moreover, the distribution of REEs between the monazite and xenotime minerals, which depends on the temperature of formation, led these phases to be used as geothermobarometer and then for the determination of the history of the related metamorphic rocks.[21,33] More importantly, these minerals have attracted much interest in the industrial field linked to the nuclear fuel cycle, whether as uranium and thorium sources (front-end) or as specific ceramics for the conditioning of highly radioactive nuclear wastes (back-end).[13,34−41] They were also proposed for the disposal of excess plutonium coming from the dismantling of nuclear weapons.[42] For both purposes, monazite and zircon were generally associated with remarkable properties, such as high resistance to aqueous leaching and radiation damage. Additionally, zircon was frequently cited as a promising inert matrix for the transmutation of minor actinides (particularly Np, Am, and Cm) in fast-neutron reactors or accelerator-driven systems.[43]

From a structural point of view, uranium and thorium are incorporated in both monazite and xenotime structures following various substitution mechanisms. The most encountered case consists of the miscibility between the monazite ($REEPO_4$) and the cheralite ($CaAn(PO_4)_2$) through

$$2REE^{3+} \leftrightarrow Ca^{2+} + An^{4+} \quad (1)$$

**Received:** August 1, 2016
**Published:** October 17, 2016





DOI: 10.1021/acs.inorgchem.6b01862
*Inorg. Chem.* 2016, 55, 11273−11282

as observed in natural minerals by Foster[44] and confirmed on synthetic compounds.[39,45] Another possibility for substitution consists of the formation of solid solutions between the monazite and isostructural $ThSiO_4$ huttonite. Such samples were reported to exist in natural phases[46] and can also be prepared as synthetic compounds, either through hydrothermal wet chemistry methods[47] or dry chemistry routes, leading to complex compositions such as the $Ln_{0.7}Th_{0.27}U_{0.03}(PO_4)_{0.7}(SiO_4)_{0.3}$ reported by McCarthy et al.[48]

In the case of the presence of $Y^{3+}$ or heavy REE, xenotime became the stable phase. According to literature, thorium and uranium could then only be incorporated through:

$$REE^{3+} + PO_4^{3-} \leftrightarrow (Th, U)^{4+} + SiO_4^{4-} \quad (2)$$

Although both xenotime and zircon compounds are crystallizing in the same structure type, there is no accurate study dedicated to the existence of a solid solution between both end-members.[28,49,50] In the latter works, all the attempts to synthesize a solid solution between xenotime and zircon have been carried out by solid-state chemistry (flux method) and only led to the partial insertion of $PO_4^{3-}$ and $REE^{3+}$ in the $ZrSiO_4$ structure type and vice versa.

In this present paper, we thus report the first synthesis of a complete solid solution $Th_{1-x}Er_x(SiO_4)_{1-x}(PO_4)_x$ (with $0 \leq x \leq 1$, by steps of 0.1) in the thorite−xenotime system. Thorium was selected as a model element for tetravalent actinides, which avoided any perturbations due to redox reactions. Also, erbium was considered as the rare earth element due to its use as a burnable poison in inert matrix fuels, which controls the reactivity toward irradiation.[51,52] All of the compounds prepared were thoroughly characterized from a structural point of view by PXRD and EXAFS. Vibrational spectroscopy features were also investigated by Raman and FTIR.

## 2. MATERIALS AND METHODS

***Caution!*** *Depleted uranium and $^{232}Th$ are α-emitters and are considered as a health risk. Experiments involving actinides require appropriate facilities and trained persons in handling of radioactive materials.*

**2.1. Synthesis.** For the synthesis of the $Th_{1-x}Er_x(SiO_4)_{1-x}(PO_4)_x$ solid solutions, the following reactants were used: $Th(NO_3)_4{\cdot}4-5H_2O$, $ErCl_3{\cdot}nH_2O$, NaOH, $NaHCO_3$, $Na_2SiO_3$. All chemicals were of analytical grade and supplied by Sigma-Aldrich. Precise and direct weighing of the exact amounts of thorium and erbium salts was precluded because of their hygroscopic character. Therefore, both salts were dissolved in acidic media. $ErCl_3$ was dissolved in 1 M HCl while the thorium chloride concentrated solution was prepared by dissolving thorium nitrate pentahydrate in concentrated HCl solution. Several cycles of evaporation and redissolution in a solution of 4 M HCl were undertaken until traces of nitrates were eliminated.[53] Concentrations of resulting solutions were finally determined by ICP-AES using a Spectro Arcos EOP device. The calibration of the apparatus was performed by the means of SPEX standard solutions diluted to concentrations varying between 0 and 15 mg $L^{-1}$.

**2.2. Powder X-ray Diffraction (PXRD).** The synthesized compounds were analyzed by PXRD with the help of a Bruker D8 advance diffractometer equipped with the Lynxeye detector and Cu Kα1,2 radiation ($\lambda$ = 1.54184 Å). The measurements were carried out in parallel geometry and with adapted sample holders (dome) in order to prevent any radioactive contamination. Each powder XRD pattern was collected in the angular range ($2\theta$) between 5° and 100° with a step of 0.019° and a total counting time of about 3 h per sample. Also, a PXRD pattern of pure silicon powder was collected in similar conditions in order to evaluate the instrumental function. In all cases only the zircon structure type[54] ($I4_1/amd$ space group) was the detected phase. Therefore, all the collected data were refined by the Rietveld method using the Fullprof_suite package.[55] During the refinements, different profile and structure parameters were allowed to vary such as the zero shift, unit-cell parameters, scale factor, and overall displacement factor. Moreover, an anisotropic size model was applied in order to evaluate the peaks broadening due to a microstructural effect. However, the occupancy of each site was fixed to the calculated values.

**2.3. Extended X-ray Absorption Fine Structure.** EXAFS measurements were performed in transmission mode at the Th $L_3$-edge (16 300 eV) and the Er $L_3$-edge (8358 eV) of $Th_{1-x}Er_x(SiO_4)_{1-x}(PO_4)_x$ samples mixed with boron nitride (BN). The measurements were carried out at the Rossendorf Beamline (BM20) dedicated to actinide-based compounds, located at the European Synchrotron Radiation Facility (ESRF; Grenoble, France). The storage ring operated at 6 GeV and 170−200 mA. For the Th $L_3$-edge, a double Si(111) 30° crystal monochromator was used for energy selection, and a pair of Rh mirrors were used for vertical beam collimation and suppression of higher-order harmonics. A gas mixture of 80% $N_2$ and 20% Ar was used in the 30 cm ionization chamber measuring the incoming beam ($I_0$), and 100% Ar gas was used to measure the beam transmitted through the sample ($I_1$) and after the respective reference foil ($I_2$), all filled at ambient pressure. For Er $L_3$-edge, a double Si(111) 0° crystal monochromator was used for energy selection combined with a pair of Si/Rh mirrors. Likewise, a gas mixture of 70% He and 30% $N_2$ was used in the ionization chamber. Energy calibration was done by measuring the absorption spectra of Y (17 038 eV) and Ni (8333 eV) metal foils placed between $I_1$ and $I_2$ parallel to the sample scans. All the samples were measured at room temperature.

Data reduction and extraction of EXAFS oscillation was performed using the Athena and Artemis package.[56] The threshold energy, $E_0$, was defined as the maximum of the first derivate of the absorption coefficient. Experimental EXAFS spectra were Fourier transformed using a Hanning window over the $k$-space ranges 2−11 $Å^{-1}$ for thorium and 2.5−11 $Å^{-1}$ for erbium. The shell fits were performed in $R$-space using $k^1$-, $k^2$-, and $k^3$-weighting for thorium and erbium. Theoretical phase shifts and backscattering amplitudes were obtained with the ab initio code FEFF8.2[57] using the $ThSiO_4$ (thorite)[2] and $ErPO_4$ (xenotime) structures[14] for thorium and erbium $L_3$-edge reported in the literature. The calculation was carried out with a radius cluster of 6 Å, taking into account all single scattering (SS) and multiple scattering (MS). During the fitting procedure, Th−O, Th···$Si_1$ ($P_2$), Th···$Si_2$ ($P_2$), and Th−Th (Er) single scattering paths (SS) were taken into account. Similarly, Er−O, Er···$P_1$ ($Si_1$), Er···$P_2$ ($Si_2$), and Er−Er (Th) SS were considered for the fitting. The distance ($R$) and Debye−Waller (DW) factor were treated as free parameters, while the coordination number ($N$) was constrained at crystallographic values. A single shift in the threshold energy ($\Delta E_0$) for each composition was varied as a global parameter. The amplitude reduction factor $S_0^2$ was obtained for $ThSiO_4$ and for $ErPO_4$ after keeping the obtained value constant through the whole composition range. To ensure transferability of phase and amplitude and to allow the estimation of systematic errors, all the data were analyzed using the same experimental phases and amplitude, filtering procedures and parameters in a similar way.

**2.4. Scanning Electron Microscopy.** SEM observations were directly conducted on powdered samples without any preparation such as metallization, using a Tescan Vega3 electronic microscope, in low-vacuum conditions (10 Pa) with an accelerating voltage of 15 kV. Additionally, the precise chemical composition of the series $Th_{1-x}Er_x(SiO_4)_{1-x}(PO_4)_x$ was analyzed by the means of energy dispersive spectrometry (EDX) coupled with an FEI Quanta 200 SEM device. In this aim, the powder was first embedded in an epoxy resin. The surface of the sample was then polished to reach an optical grade and metalized by carbon coating. Experimental data were finally collected from about 50 different locations of the sample surface, considering $ThO_2$, $ErPO_4$, and $NaAlSi_3O_8$ as internal standards for the elements Th, Er, P, and Si, respectively.

**2.5. Vibrational Spectroscopy.** Raman spectra were recorded in the 100−1500 $cm^{-1}$ range by the means of a Horiba−Jobin Yvon Aramis apparatus equipped with an edge filter and using a He−Ne



DOI: 10.1021/acs.inorgchem.6b01862
Inorg. Chem. 2016, 55, 11273−11282

laser (633 nm) delivering 10 mW on the sample surface. The laser beam was then focused on a small fraction of powdered sample simply deposited on a glass lamella using an Olympus BX 41 microscope. The scattered Raman light was collected in a 180° backscattering geometry and dispersed by a grating of 1800 grooves/mm after having passed a 150 $\mu$m entrance slit, resulting in a spectral resolution lower than 1 $cm^{-1}$. For each spectrum, a dwell time of 30 s was considered with an average of 10 scans. Before analysis, the apparatus was calibrated with a silicon wafer, using the first-order Si line at 520.7 $cm^{-1}$.

FTIR spectra were recorded in the 380−4000 $cm^{-1}$ range thanks to a Perkin-Elmer FTIR Spectrum 100 device. Powdered samples were deposited at the surface of an ATR crystal without any prior preparation. The spectra collected in such operating conditions exhibited a resolution lower than 2 $cm^{-1}$.

## 3. RESULTS AND DISCUSSION

**3.1. Synthesis and SEM/EDX Characterization.** First attempts to prepare $Th_{1-x}Er_x(SiO_4)_{1-x}(PO_4)_x$ solid solutions were performed by following several methods previously reported in the literature for the synthesis of rhabdophane or xenotime-type compounds.[58] The first protocol considered consisted of the direct coprecipitation of the reactants in aqueous solution. A starting mixture of thorium and erbium in the desired stoichiometric ratio was then poured in a solution containing 5 M $H_3PO_4$ and dissolved $Na_2SiO_3$ and then transferred to a Teflon container at 90 °C for 2 weeks. Nevertheless, the PXRD pattern analysis of the resulting powder (not presented here) showed the formation of an amorphous gel whatever the chemical composition considered. The second method consisted of a heat treatment of the previous mixtures at 250 °C. However, this chemical route also failed yielding to a polyphase system composed mainly of thorite ($ThSiO_4$) and Er-xenotime ($ErPO_4$).

Finally, powdered samples of $Th_{1-x}Er_x(SiO_4)_{1-x}(PO_4)_x$ solid solutions were prepared by using a method recently reported in the literature for the synthesis of coffinite $USiO_4$,[59] in modification of the protocol initially proposed by Hoekstra and Fuchs.[8] The calculated amount of $Na_2SiO_3$ was dissolved in deionized water and mixed with a desired amount of 5 M $H_3PO_4$. In parallel, weighed amounts of Th and Er acidic solutions were mixed and then poured slowly into the anionic solution under continuous stirring. Then, the pH of the solution was raised by adding 8 M NaOH dropwise to the target value ranging between 11 and 11.5. Afterward, the solution was buffered to 8.7 ± 0.1 by adding $NaHCO_3$. The final solution was transferred into a Teflon-lined acid digestion bomb (Parr) and placed in an oven for 1 week at 250 °C. All of the reactions were carried out in a fume hood in air. The precipitate collected after this treatment was separated from the supernatant by centrifugation at 4500 rpm, washed twice with deionized water and ethanol, and then finally dried overnight at 90 °C.

For all of the studied samples, the powders were found to consist of small needle-like crystals. The size of these grains was typically in the 200−800 nm range, but no clear trend was established versus the erbium weight loading. Figure 1 shows selected micrographs of four different compositions. The analysis of the synthesized powders by EDX confirmed the formation of samples with the presence of Th, Er, Si, and P within the structure. The trend of the measured values confirms the formation of a solid solution as shown in Table 1. Regarding the reported results, we observed a small and systematic deviation of the measured values compared to the calculated ones, still acceptable as experimental errors. The values obtained for phosphorus had a systematic underestimation of about 5% of P atomic percentage. This problem is a recurrent one on all our phosphate-based compounds which is mainly due to a bias caused by the standardization method. Moreover, attempts to perform a total dissolution of the powders in aqua regia were unsuccessful because of the precipitation of amorphous silica which made difficult the collection of reliable data.

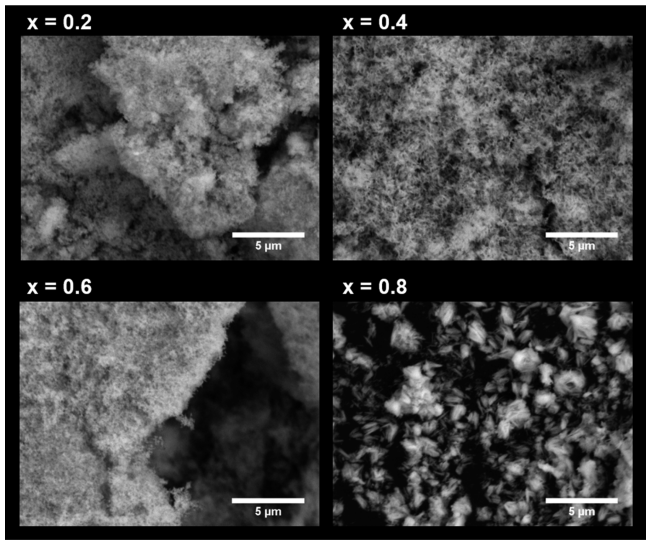


**Figure 1.** SEM micrographs of the $Th_{1-x}Er_x(SiO_4)_{1-x}(PO_4)_x$ solid solutions.

**Table 1. EDX Compositions Determined for $Th_{1-x}Er_x(SiO_4)_{1-x}(PO_4)_x$ Solid Solutions**

| $x_{calc}$ | $x$Er | $x$Th | $x$P | $x$Si | (Er + Th)/(Si + P) |
|---|---|---|---|---|---|
| 0.0 | 0 | 1 | 0 | 1 | |
| 0.1 | 0.12(1) | 0.88(1) | 0.05(2) | 0.95(2) | 1.1(1) |
| 0.2 | 0.24(2) | 0.76(2) | 0.16(2) | 0.84(2) | 1.2(1) |
| 0.3 | 0.36(1) | 0.64(1) | 0.27(1) | 0.73(1) | 1.2(1) |
| 0.4 | 0.44(2) | 0.56(2) | 0.35(1) | 0.65(1) | 1.2(1) |
| 0.5 | 0.56(3) | 0.47(3) | 0.45(1) | 0.55(1) | 1.2(1) |
| 0.6 | 0.57(1) | 0.43(1) | 0.53(1) | 0.47(1) | 1.3(1) |
| 0.7 | 0.75(3) | 0.25(3) | 0.70(1) | 0.30(1) | 1.2(1) |
| 0.8 | 0.81(3) | 0.19(3) | 0.74(1) | 0.26(1) | 1.1(1) |
| 0.9 | 0.89(1) | 0.11(1) | 0.86(1) | 0.14(1) | 1.1(1) |
| 1.0 | 1 | 0 | 1 | 0 | |

**3.2. Structural Characterization.** *PXRD.* All of the prepared powdered samples were analyzed by PXRD (Figure 2a). Systematically, only the zircon structure type was observed, conversely to the case of uranothorite ($Th_{1-x}U_xSiO_4$),[10,11] which led to the formation of mixed phases with the simultaneous stabilization of nanometric $Th_{1-y}U_yO_2$ and $SiO_2$ by-products. Given those results, the reactions performed under hydrothermal conditions at 250 °C have led to the formation of a single pure phase crystallizing in the zircon structure type which corresponds to the expected $Th_{1-x}Er_x(SiO_4)_{1-x}(PO_4)_x$ solid solution. All these compounds crystallize in the tetragonal system, with a space group of $I4_1/amd$ (general view of the structure down the $c$ axis presented in Figure 3). In this system, both end-members, namely, $ThSiO_4$,[2,60] and $ErPO_4$,[61] are well-known and isostructural but generally differ in their method of synthesis.



DOI: 10.1021/acs.inorgchem.6b01862
Inorg. Chem. 2016, 55, 11273−11282

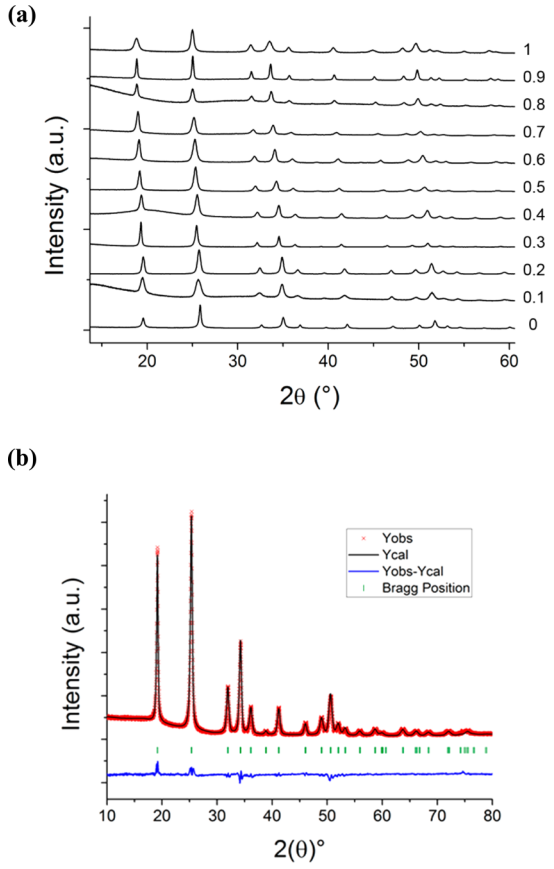


**Figure 2.** (a) PXRD patterns of the $Th_{1-x}Er_x(SiO_4)_{1-x}(PO_4)_x$ solid solution showing a shift toward low angles when increasing erbium loading. (b) Observed, calculated, and difference curves obtained during the Rietveld refinement of the PXRD pattern of the $x = 0.5$ sample.

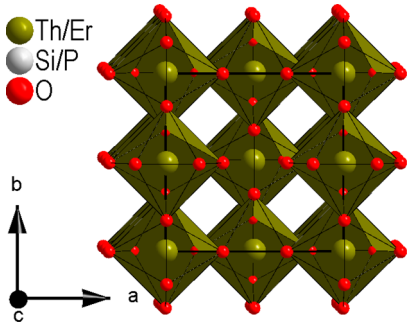


**Figure 3.** General view of the zircon structure type down the $c$ axis.

The analysis of the patterns reported in Figure 2a evidenced a shift in the XRD lines toward the low angles ($2\theta$) depending on the erbium content. The experimental unit-cell parameters, refined using Rietveld methods, are reported in Table 2 while Figure 2b shows the observed, calculated, and difference curves for the compound $Th_{0.5}Er_{0.5}(SiO_4)_{0.5}(PO_4)_{0.5}$ refined in the zircon structure type. Moreover, the linear variation of the unit-cell volume versus the erbium content, viewed in Figure 4, appears in agreement with Vegard's law. At first glance, this variation appears to be in agreement with crystal ionic radius reported in the Shannon tables for $Th^{4+}$ and $Er^{3+}$ in coordination eight with $r = 1.19$ and 1.144 Å, respectively. Moreover, we should also consider the size of $Si^{4+}$ (0.4 Å) and $P^{5+}$ (0.3 Å) in the structure. From the microscopic point of

**Table 2. Refined Unit-Cell Parameters for the $Th_{1-x}Er_x(SiO_4)_{1-x}(PO_4)_x$ Solid Solution**

| $x_{calc}$ | $a$ (Å) | $c$ (Å) | $V$ (Å$^3$) |
|---|---|---|---|
| 0.0 | 7.1443(2) | 6.3240(2) | 322.79(1) |
| 0.1 | 7.1177(1) | 6.2882(1) | 318.57(1) |
| 0.2 | 7.1070(2) | 6.2602(2) | 316.20(2) |
| 0.3 | 7.0761(3) | 6.2321(3) | 312.06(2) |
| 0.4 | 7.0539(2) | 6.1986(3) | 308.43(2) |
| 0.5 | 7.0361(3) | 6.1627(3) | 305.10(2) |
| 0.6 | 7.0132(2) | 6.1308(2) | 301.55(1) |
| 0.7 | 6.9943(2) | 6.1004(2) | 298.44(1) |
| 0.8 | 6.9683(2) | 6.0671(2) | 294.61(1) |
| 0.9 | 6.9288(3) | 6.0401(3) | 289.98(2) |
| 1.0 | 6.8837(1) | 6.0227(1) | 285.39(1) |

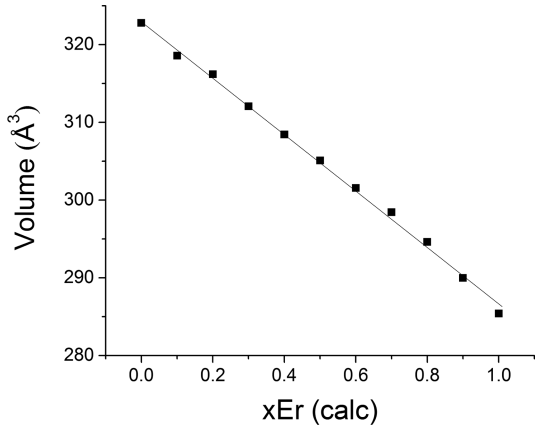


**Figure 4.** Variation of the unit-cell volume (Å$^3$) in the $Th_{1-x}Er_x(SiO_4)_{1-x}(PO_4)_x$ system.

view, it seems that the formed solid solution exhibits a perfectly random distribution between the elements in both Th/Er and Si/P sites inside the structure. In order to obtain more information and details, EXAFS experiments were performed to probe the local structure as detailed below.

*Local Structure.* For clarification of the behavior of erbium and its influence on the host $ThSiO_4$, the local structure of thorium and erbium in all the $Th_{1-x}Er_x(SiO_4)_{1-x}(PO_4)_x$ samples prepared was systematically investigated by EXAFS at Th and Er $L_3$-edges. The $k^3$-weighted EXAFS spectra and their Fourier transforms (FTs) obtained for the 10 different compositions are shown in Figure 5a,b for the Th and Er $L_3$-edges, respectively.

The FT obtained for the $ThSiO_4$ end-member ($x = 0$) at the Th $L_3$-edge shows a first shell around the thorium atom consisting of eight oxygen contributions at 2.4 Å. The next neighbor contributions at 3.20 and 3.95 Å were attributed to the single scattering contribution of two $Si_1$ and four $Si_2$ atoms in the thorite structure, respectively. Additionally, a cation–cation contribution related to the Th–Th was fitted at 3.93 Å. Besides, the FT determined for $ErPO_4$ ($x = 1$) at the Er $L_3$-edge (Figure 5b) also shows the eight oxygen contributions in the first coordination shell at 2.34 Å. In the same way as that for $ThSiO_4$, the FT of $ErPO_4$ presents a second and a third peak related to the single scattering contribution of two $P_1$ at 3.03 Å and four $P_2$ at 3.88 Å. For the $ErPO_4$ end-member, it was also possible to fit two Er–Er distances, at 3.76 and 5.69 Å. For the rest of the compositions, the longest Er contribution was no longer observable. These values are shown in the Table 3 and


DOI: 10.1021/acs.inorgchem.6b01862
Inorg. Chem. 2016, 55, 11273–11282

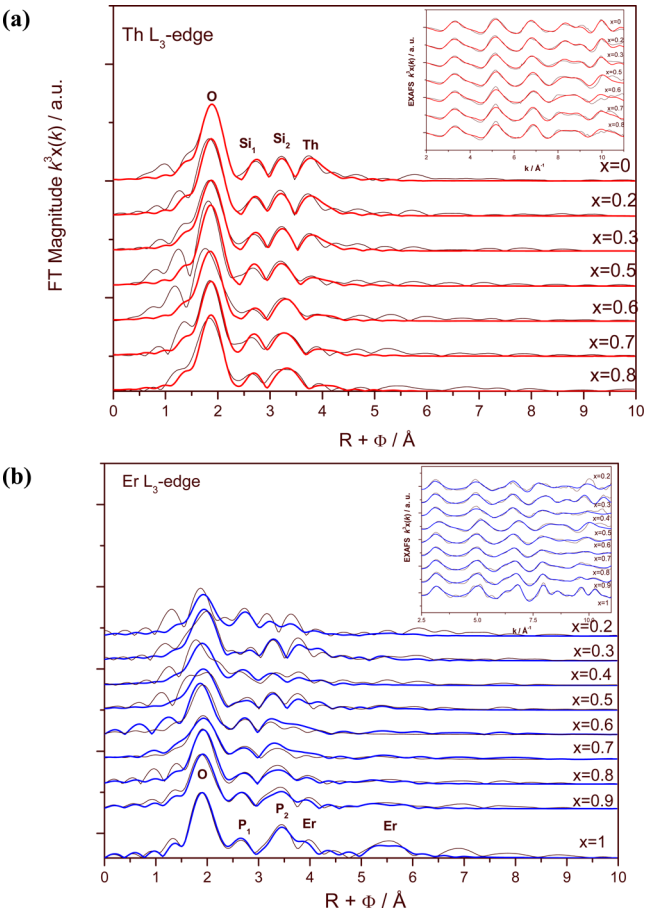


**Figure 5.** Experimental $k^3\chi(k)$ EXAFS spectra of $Th_{1-x}Er_x(SiO_4)_{1-x}(PO_4)_x$ solid solutions and their respective Fourier transforms (FTs) at the (a) Th $L_3$-edge and (b) Er $L_3$-edge. Colored lines are the best fit achieved; black lines are the experimental data. FT peak positions are not corrected for phase shifts.

were found to be in agreement with the average crystal diffraction distances reported in the literature.[2,14,60]

For intermediate solid solutions, the FT measurements at the Th $L_3$-edge from $x = 0$ to $x = 0.5$ (Figure 5a) showed little changes on the local environment around Th. However, starting from $x = 0.5$ to $x = 0.8$, the amplitude of Th peak contribution decreased whereas a broadening on the $Si_2$ peaks was revealed. Such behavior might be related to the shortening of Th−Th(Er) distances as actinide content decreased and/or to interferences between the two Er and Th scattering paths resulting in the attenuation of the cation−cation FT peak. The EXAFS spectra for the Th $L_3$-edge showed no modification at lower $k$-ranges. However, small modifications started at 8 $Å^{-1}$, which is probably due to the mixing backscattering between Th and Si atoms. Conversely, the FTs of $Th_{1-x}Er_x(SiO_4)_{1-x}(PO_4)_x$ solid solutions at Er $L_3$-edge (Figure 5b) showed more significant changes in the local environment around Er than those of the Th $L_3$-edge at higher Er content ($x = 0.9$). Such modifications were also revealed in their EXAFS spectra, where a bigger change in the atomic structure around the xenotime $ErPO_4$ was observed as Th content increased.

*Cation Oxygen Environment.* According to the criteria for isovalent solid solutions, the bond length could be limited by two cases, which will reflect their ability to adapt to the host structure. The first is *no relaxation* in the system, which assumes that the atomic radii are approximately conserved and independent of the composition of the solid solution (Pauling's concept). In contrast, the second corresponds to *full relaxation* in the system, where the virtual crystal approximation (VCA) is valid and bond lengths follow Vegard's law.[62]

The cation−oxygen interatomic distances are presented in Figure 6, with respective error bars calculated from the difference of EXAFS values and the distances of the crystal structure mentioned already. The derived Th−O and Er−O bond length distances showed that Th−O and Er−O distances are element-specific due to the difference in their crystal effective radius (1.144 Å for Er and 1.19 Å for Th). The Er−O bond length determined by EXAFS increased in the zircon-type structure with the thorium content. However, the individual Th−O bond length remained close to the value determined in pure $ThSiO_4$ (2.39 Å); i.e., there is no relaxation. It suggests that Th−O bond lengths are preserved in the first coordination shell as erbium content increases, due to its strong covalent bond. From these results, the host zircon-type structure ($ErPO_4$) is modified with the change in the actinide content (i.e., full relaxation).[63] Besides, the average EXAFS distance plotted in Figure 6 showed a similar trend compared to the PXRD results (Figure 4). Another observation is that the Debye−Waller factor ($\sigma^2$) in the Er−O coordination shell is increasing with thorium content, going from 0.005 50 to 0.0100 $Å^2$. However, the $\sigma^2$ values for the Th−O contribution remained at the same scale, with an average of 0.006 $Å^2$. Note that this reflects the thermal and static contribution since measurements were performed at room temperature.

*Cation−Cation Environment.* The cation−cation distribution was determined with a single broad peak within the EXAFS resolution. The variation in the second neighbor distribution is presented in Figure 7 with the corresponding error bars. First, the Er−Er (Th) and Th−Th (Er) distances are approximatively equal to their average distances, as reported previously in the case of covalent and ionic systems.[63,64] Second, with a look at the Er−Er (Th) local environment, a change from 3.76 to 3.94 Å was observed. Nonetheless, the Th−Th (Er) local environment suffered a small variation from 3.93 to 3.90 Å. These results again suggest that although the Er local structure was modified, that of Th remained close to that of pure thorite ($ThSiO_4$). This kind of behavior was already reported for stabilized zirconia with actinides.[65,66] In addition, as the thorium content increased, the Er−Er (Th) bond length distances became similar to the Th−Th ones. Finally, Figure 8 shows the variation in the Er−P and Th−Si interatomic distances. It is important to mention that P and Si are undistinguishable by EXAFS because of their close atomic number. However, from fitting, it was observed that Th−Si and Er−P distances remained almost constant, meaning that there is a less significant change in their distances than those obtained for the cations.

**3.3. Vibrational Spectroscopy.** The vibrational features of $XO_4$ anions within a zircon-type structure have been widely described, either in the case of phosphate species for the xenotime,[67] or for silicates in actinide-based compounds such as thorite[68] or coffinite.[9] The factor-group analysis based on the irreducible representation of the $D_{4h}$ point group leads to the optical vibrations as follows:

$$\Gamma = 2A_{1g} + 2A_{2g} + 4B_{1g} + B_{2g} + 5E_g + A_{1u} + 3A_{2u} + B_{1u} + 2B_{2u} + 4E_u \quad (3)$$



DOI: 10.1021/acs.inorgchem.6b01862
Inorg. Chem. 2016, 55, 11273−11282

Table 3. $Th_{1-x}Er_x(SiO_4)_{1-x}(PO_4)_x$ Fit Results for the Main Coordination Shells at the Th and Er $L_3$-Edges

| | Th−O | | $Th\cdots Si_1$ | | $Th\cdots Si_2$ | | Th···Th | | |
|---|---|---|---|---|---|---|---|---|---|
| $x$ | $R$/Å | $\sigma^2$/Å$^2$ | $R$/Å | $\sigma^2$/Å$^2$ | $R$/Å | $\sigma^2$/Å$^2$ | $R$/Å | $\sigma^2$/Å$^2$ | |
| 0 | 2.40 | 0.0058 | 3.20 | 0.0045 | 3.95 | 0.0077 | 3.93 | 0.0042 | $S_0^2$ = 0.81 |
| | (8) | (13) | (25) | (36) | (36) | (51) | (16) | (18) | % $R$-factor = 2.0 |
| | | | | | | | | | $E_0$ = 10.88 |
| 0.2 | 2.39 | 0.0057 | 3.18 | 0.0046 | 3.95 | 0.0061 | 3.92 | 0.0044 | % $R$-factor = 1.1 |
| | (6) | (7) | (22) | (29) | (26) | (35) | (14) | (15) | $E_0$ = 10.16 |
| 0.3 | 2.40 | 0.0067 | 3.19 | 0.0050 | 3.95 | 0.0050 | 3.93 | 0.0056 | % $R$-factor = 1.4 |
| | (5) | (8) | (25) | (33) | (24) | (32) | (17) | (19) | $E_0$ = 10.37 |
| 0.4 | 2.38 | 0.0049 | 3.19 | 0.0102 | 3.92 | 0.0045 | 3.90 | 0.0078 | % $R$-factor = 2.8 |
| | (7) | (11) | (71) | (12) | (39) | (53) | (40) | (50) | $E_0$ = 10.37 |
| 0.5 | 2.38 | 0.0053 | 3.16 | 0.0033 | 3.93 | 0.0036 | 3.91 | 0.0084 | % $R$-factor = 2.2 |
| | (9) | (8) | (26) | (36) | (29) | (37) | (37) | (45) | $E_0$ = 9.75 |
| 0.6 | 2.38 | 0.0069 | 3.17 | 0.0084 | 3.94 | 0.0018 | 3.90 | 0.0085 | % $R$-factor = 2.9 |
| | (9) | (11) | (50) | (80) | (25) | (30) | (43) | (45) | $E_0$ = 9.75 |
| 0.7 | 2.39 | 0.0062 | 3.16 | 0.0022 | 3.95 | 0.0014 | 3.92 | 0.0080 | % $R$-factor= 2.5 |
| | (10) | (11) | (22) | (30) | (23) | (27) | (35) | (43) | $E_0$ = 10.49 |
| 0.8 | 2.39 | 0.0060 | 3.16 | 0.0039 | 3.95 | 0.0010 | 3.90 | 0.0074 | % $R$-factor = 2.1 |
| | (9) | (10) | (27) | (39) | (21) | (24) | (33) | (39) | $E_0$ = 10.47 |
| | Er−O | | $Er\cdots P_1$ | | $Er\cdots P_2$ | | Er···Er | | |
| $x$ | $R$/Å | $\sigma^2$/Å$^2$ | $R$/Å | $\sigma^2$/Å$^2$ | $R$/Å | $\sigma^2$/Å$^2$ | $R$/Å | $\sigma^2$/Å$^2$ | |
| 0 | | | | | | | | | $S_0^2$ = 0.77 |
| 0.2 | 2.38 | 0.0111 | 3.08 | 0.0012 | 3.88 | 0.0101 | 3.94 | 0.0101 | % $R$-factor = 4.4 |
| | (14) | (16) | | | | | (54) | | $E_0$ = 15.47 |
| 0.3 | 2.36 | 0.0078 | 3.05 | 0.0073 | 3.83 | 0.0041 | 3.98 | 0.0041 | % $R$-factor = 2.5 |
| | (9) | (10) | (29) | (43) | (23) | (14) | (16) | (14) | $E_0$ = 14.69 |
| 0.4 | 2.35 | 0.0105 | 3.05 | 0.0040 | 3.84 | 0.0084 | 3.98 | 0.0084 | % $R$-factor = 4.1 |
| | (10) | (12) | (25) | (26) | (38) | (38) | (40) | (38) | $E_0$ = 14.28 |
| 0.5 | 2.36 | 0.0108 | 3.05 | 0.0088 | 3.83 | 0.0066 | 3.97 | 0.0066 | % $R$-factor= 3.5 |
| | (10) | (14) | (33) | (58) | (30) | (23) | (24) | (23) | $E_0$ = 14.77 |
| 0.6 | 2.35 | 0.0086 | 3.06 | 0.0047 | 3.83 | 0.0102 | 3.96 | 0.0102 | % $R$-factor = 3.2 |
| | (10) | (11) | (22) | (35) | (42) | (45) | (42) | (45) | $E_0$ = 14.40 |
| 0.7 | 2.36 | 0.0100 | 3.06 | 0.0067 | 3.85 | 0.0110 | 3.95 | 0.0110 | % $R$-factor = 2.3 |
| | (8) | (10) | (22) | (30) | (35) | (36) | (34) | (36) | $E_0$ = 15.00 |
| 0.8 | 2.35 | 0.0074 | 3.05 | 0.0070 | 3.89 | 0.0100 | 3.78 | 0.0100 | % $R$-factor = 2.2 |
| | (7) | (9) | (24) | (38) | (63) | (35) | (62) | (35) | $E_0$ = 14.74 |
| 0.9 | 2.35 | 0.0073 | 3.04 | 0.0036 | 3.89 | 0.0096 | 3.77 | 0.0096 | % $R$-factor = 2.3 |
| | (8) | (9) | (18) | (25) | (51) | (26) | (53) | (51) | $E_0$ = 15.02 |
| 1.0 | 2.34 | 0.0055 | 3.03 | 0.0018 | 3.88 | 0.0049 | 3.76 | 0.0049 | % $R$-factor = 2.3 |
| | (7) | (8) | (16) | (19) | (34) | (11) | (22) | (11) | $E_0$ = 14.97 |

Among these vibration modes, 12 are Raman-active and split between the 7 internal vibrations of the $XO_4$ tetrahedra ($\Gamma_{int}$) and 5 external modes corresponding to the motion of solid tetrahedral in the unit cell ($\Gamma_{ext}$), such as

$$\Gamma_{int} = 2A_{1g} + 2B_{1g} + B_{2g} + 2E_g \quad (4)$$

$$\Gamma_{ext} = 2B_{1g} + 3E_g \quad (5)$$

Similarly, FTIR-active vibration modes can be described as

$$\Gamma_{int} = A_{1u} + 2A_{2u} + 2B_{2u} + 2E_u \quad (6)$$

$$\Gamma_{ext} = A_{2u} + B_{1u} + 2E_u \quad (7)$$

The Raman spectra recorded for the $Th_{1-x}Er_x(SiO_4)_{1-x}(PO_4)_x$ solid solutions generally appeared in good agreement with this factor-group analysis (Figure 9). For the $ErPO_4$ end-member, the 7 vibration modes of the phosphate tetrahedra (numbered after the nomenclature employed by Kolesov et al.[69]) were observed at 334 and 473 cm$^{-1}$ ($\nu_2$: symmetric bending), 590 and 665 cm$^{-1}$ ($\nu_4$: antisymmetric bending), 999 cm$^{-1}$ ($\nu_1$: symmetric stretching), and 1021 and 1057 cm$^{-1}$ ($\nu_3$: antisymmetric stretching), along with the rotational external vibration at 296 cm$^{-1}$. These results match the previous works undertaken on Er-based xenotime,[67,70] although the position of the vibration bands appears to be slightly modified, probably due to the presence of interference bands between 400 and 850 cm$^{-1}$. This rogue signal corresponds to the red luminescence emission of $Er^{3+}$ at 652 nm, from the $^4F_{9/2} \rightarrow {}^4I_{15/2}$ transition.[71,72] On the other hand, only 4 internal vibration modes of the silicate group were observed in the thorite end-member, at 438 ($\nu_2$), 592 ($\nu_4$), 887 ($\nu_1$), and 914 cm$^{-1}$ ($\nu_3$). Nevertheless, such a discrepancy was already reported by several authors and correlated to the existence of interactions between $SiO_4$ tetrahedra and the metallic cation.[68] In this case, silicate units cannot be treated strictly independently, resulting in fewer internal vibration modes than predicted by the factor-group analysis.

Between these two extreme cases, the Raman spectra recorded for the xenotime−thorite solid solutions exhibit the vibrational features of both structures, although with notable



DOI: 10.1021/acs.inorgchem.6b01862
Inorg. Chem. 2016, 55, 11273−11282

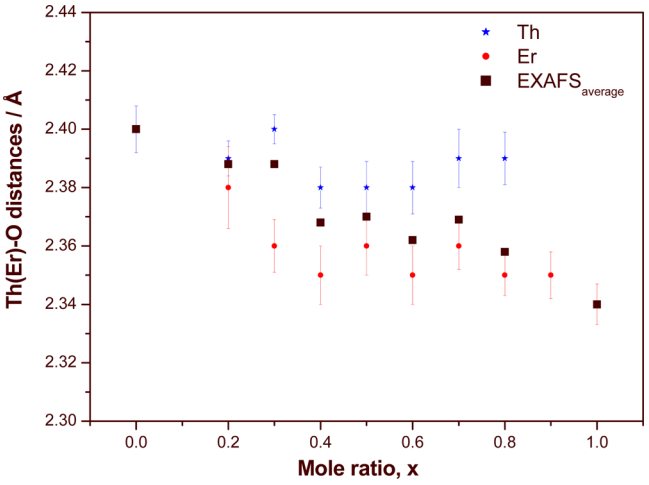


**Figure 6.** Interatomic distances Th−O (upper ■) and Er−O (bottom ★) vs composition in $Th_{1-x}Er_x(SiO_4)_{1-x}(PO_4)_x$ solid solutions. The square symbols represents the average value obtained by EXAFS.

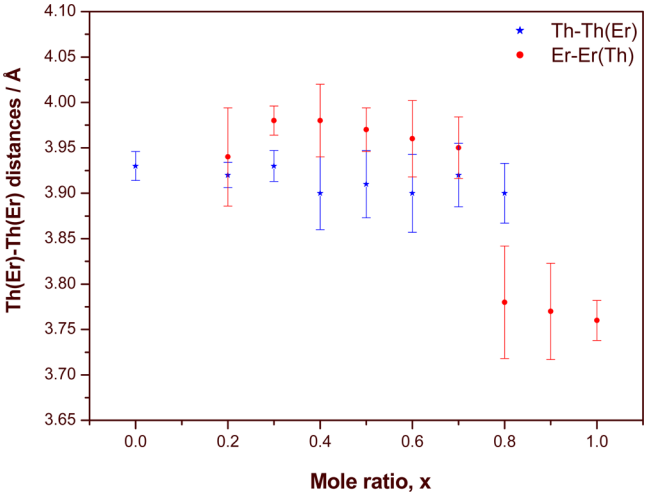


**Figure 7.** Variation in the interatomic distances Th−Th(Er) (★) and Er−Er(Th) (●) vs composition in $Th_{1-x}Er_x(SiO_4)_{1-x}(PO_4)_x$ solid solutions.

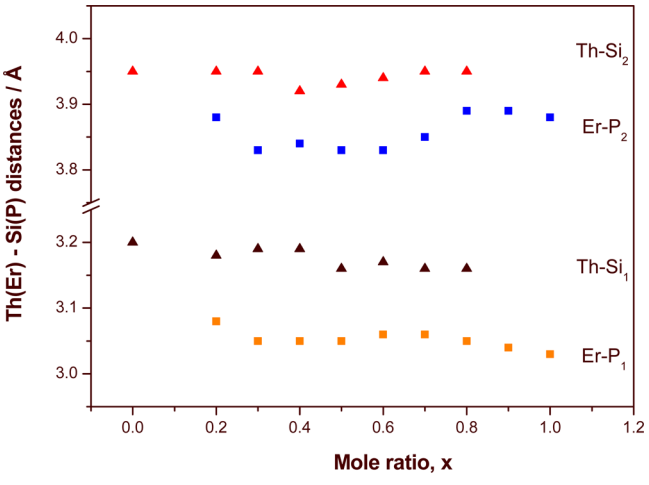


**Figure 8.** Variation in the interatomic distances Th(Er)−Si(P) vs composition in $Th_{1-x}Er_x(SiO_4)_{1-x}(PO_4)_x$ solid solutions.

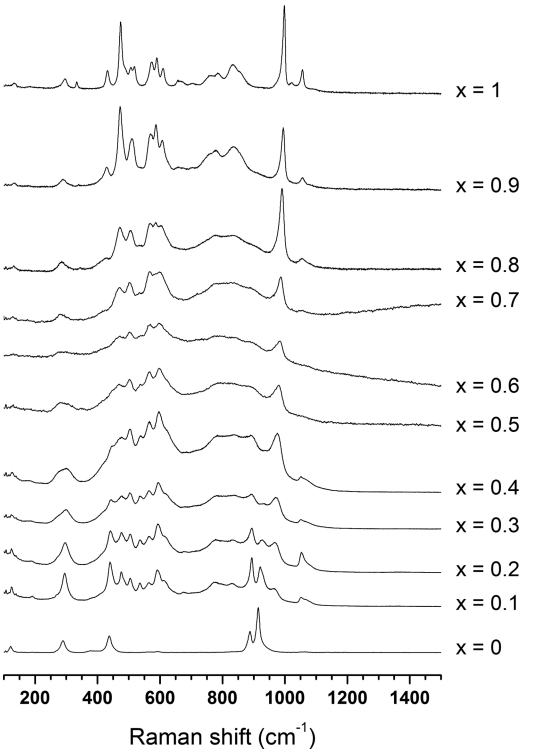


**Figure 9.** Raman spectra of the $Th_{1-x}Er_x(SiO_4)_{1-x}(PO_4)_x$ solid solutions in the 100−1500 $cm^{-1}$ range.

variations in their relative intensities. Indeed, the modes related to silicate units rapidly vanished when decreasing the thorium content in the sample, and were almost undetectable for $x <$ 0.7. This phenomenon probably arose from the better response of phosphate tetrahedra in Raman spectroscopy, but also from the progressive incorporation of erbium in the sample which induced an increasing parasite emission in the $\nu_2(SiO_4)$ and $\nu_4(SiO_4)$ zone. The same applies for the $PO_4$ bending mode in this region of the spectra. Conversely, it appeared easier to follow the variation of the phosphate stretching modes which remained visible whatever the thorium incorporation rate ($x$). On this basis, the $\nu_1$ vibration band was fitted thanks to the Jandel Peakfit software, using a pseudo-Voigt function with a Gaussian−Lorenzian ratio systematically higher than 0.7. By this means, correlation coefficients $r^2$ greater than 0.992 were usually obtained, and allowed us to plot the variation of the $\nu_1$ Raman shift versus $x$ (Figure 10). This latter was found to follow a linear trend, with

$$\sigma(\nu_1) = 964 + 33 \times x \quad (8)$$

Such linear variation of the $XO_4$ stretching mode was already pointed out in the case of cationic substitutions within zircon-type silicates, such as $Zr_{1-x}Hf_xSiO_4$,[73] $Zr_{1-x}U_xSiO_4$,[74] and $Th_{1-x}U_xSiO_4$.[9] However, it has never been mentioned, to our knowledge, in the case of coupled substitutions that involve modifications on both cationic and anionic sites. Moreover, this linear behavior appears in good agreement with the formation of a complete solution between $ErPO_4$ xenotime and $ThSiO_4$ thorite. Indeed, with the progressive substitution of $Th^{4+}$ by $Er^{3+}$, and simultaneously that of silicate units by phosphate groups, leading to the shrinkage of the quadratic unit cell, one can expect the P−O bond length to decrease, and then there is an increase in the vibration frequency. Also, one can note that the progressive replacement of erbium by thorium, on one


DOI: 10.1021/acs.inorgchem.6b01862
Inorg. Chem. 2016, 55, 11273−11282

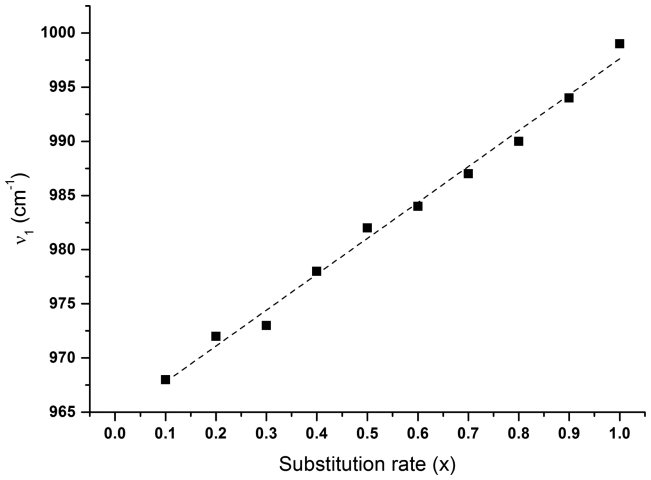


**Figure 10.** Variation of the $\nu_1$ vibration position versus $x$ in the Raman spectra of the $Th_{1-x}Er_x(SiO_4)_{1-x}(PO_4)_x$ solid solutions.

hand, and of phosphate by silicate, on the other, led the $\nu_1$ vibration band to widen progressively. Since the PXRD study did not provide evidence of any significant influence of the substitution on the crystallization state of the samples, the broadening of the signal might reflect a modification of the $PO_4$ polyhedra. In these conditions, the phosphate tetrahedrons not only shrink, but are also probably distorted, leading to the apparition of additional vibration modes overlapping with the initial $\nu_1$ vibration.

These results were confirmed by the data obtained by FTIR spectroscopy (Figure 11), which again exhibited the characteristic vibration modes usually described for xenotime and thorite end-members. Moreover, the better sensitivity of the silicate units to FTIR compared with Raman, as well as the absence of interfering luminescence phenomena, offered the possibility to directly compare the modifications in the relative intensities of the $SiO_4$ and $PO_4$ stretching modes. Hence, the progressive substitution of the anionic species along the $Th_{1-x}Er_x(SiO_4)_{1-x}(PO_4)_x$ solid solution led to the apparition of a crossing point at around 910 cm$^{-1}$. In this case, vibrational spectroscopy can thus be used to roughly estimate the chemical composition of the solid.

## 4. CONCLUSION

The incorporation of actinides in potential conditioning matrices such as phosphates or silicates remains a very important point to examine from a chemical point of view. Although several protocols are reported in the literature on the basis of the use of solid-state chemistry methods at high temperature, these methods, due to a lack in the reactivity of the powders or insufficient homogenization during the mixing or grinding steps, can lead to the presence of less durable secondary phases during leaching tests. On the contrary, the development of wet chemistry routes is considered as a promising alternative method to obtain directly the target matrices at lower temperature and with an improved homogeneity. For this purpose, pure powdered compounds $Th_{1-x}Er_x(SiO_4)_{1-x}(PO_4)_x$ belonging to the zircon−xenotime structure type were successfully synthesized under hydrothermal conditions ($T$ = 250 °C, $t$ = 7 days) in application of the recent protocol used for the synthesis of the coffinite.[59] The characterization by SEM (EDX) and PXRD confirmed the formation of a complete solid solution over the whole composition range in agreement with Vegard's law. The crystal structure of these solids exhibited a linear decrease of the unit-cell volume as a function of the erbium/phosphate content. However, the analysis of the local structure in particular with EXAFS measurements shows that the Th−O distances do not evolve so much during the erbium to thorium substitution and remain close to those found for the thorite end-member ($ThSiO_4$). On the contrary, the Er−O−(P,Si) sequence suffers more than Th−O−(P,Si) during the (Th, $SiO_4$) ⇔ (Er, $PO_4$) substitution, by showing a large increase of the Er−O distance when increasing the thorium content in the structure.

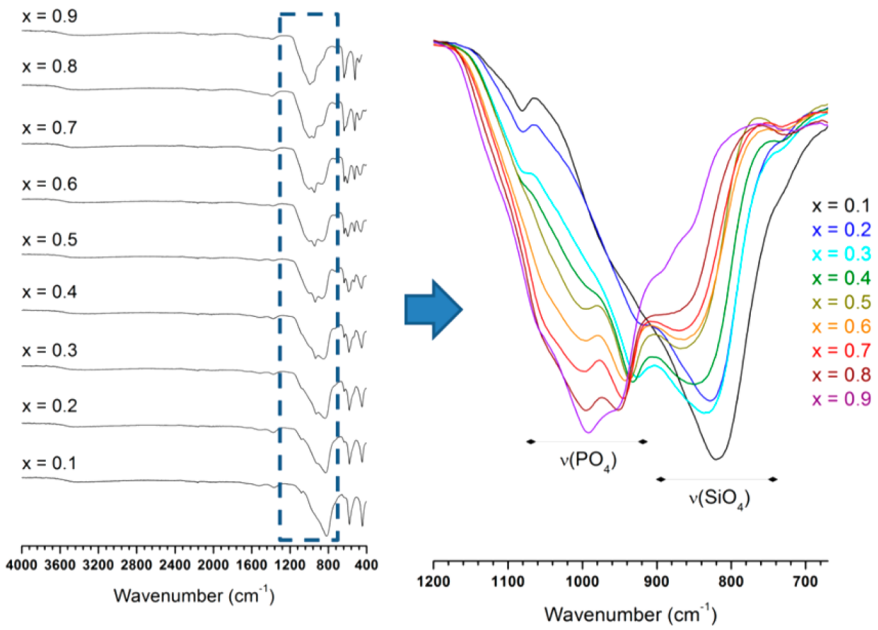


**Figure 11.** FTIR spectra of the $Th_{1-x}Er_x(SiO_4)_{1-x}(PO_4)_x$ solid solutions in the 400−4000 cm$^{-1}$ range, with focus on the 650−1200 cm$^{-1}$ range showing the stretching modes of the $XO_4$ tetrahedrons.



DOI: 10.1021/acs.inorgchem.6b01862
*Inorg. Chem.* 2016, 55, 11273−11282

Correlatively, a distortion of the phosphate groups was observed by spectroscopy.

## AUTHOR INFORMATION


### Corresponding Author

*E-mail: adel.mesbah@cea.fr.


### Notes

The authors declare no competing financial interest.

## ACKNOWLEDGMENTS

The authors would like to thank C. Gausse, P. H. Imbert, and J. M. Sandate Dominguez for their help in the preparation of the samples and EXAFS measurements. They are also grateful to R. Podor for supporting EDX/experiments.

## REFERENCES


(1) Mooney, R. C. L. Crystal structures of a series of rare earth phosphates. *J. Chem. Phys.* **1948**, *16* (10), 1003−1003.

(2) Taylor, M.; Ewing, R. C. Crystal-structures of $ThSiO_4$ polymorphs - huttonite and thorite. *Acta Crystallogr., Sect. B: Struct. Crystallogr. Cryst. Chem.* **1978**, *34* (APR), 1074−1079.

(3) Pabst, A. Huttonite, a New Monoclinic Thorium Silicate. *Am. Mineral.* **1951**, *36* (1−2), 60−65.

(4) Keller, C. Untersuchung ueber die germinate und silicate des types $ABO_4$ de vieuvertigen elemente thorium bis americium. *Nukleonik* **1963**, *5*, 41−48.

(5) Clavier, N.; Podor, R.; Dacheux, N. Crystal chemistry of the monazite structure. *J. Eur. Ceram. Soc.* **2011**, *31* (6), 941−976.

(6) Fuchs, L. H. Formation and Properties of Synthetic Thorite Crystals. *Am. Mineral.* **1958**, *43* (3−4), 367−368.

(7) Fuchs, L. H.; Gebert, E. X-Ray Studies of Synthetic Coffinite, Thorite and Uranothorites. *Am. Mineral.* **1958**, *43* (3−4), 243−248.

(8) Hoekstra, H. R.; Fuchs, L. H. Synthesis of Coffinite—$USiO_4$. *Science* **1956**, *123* (3186), 105−105.

(9) Clavier, N.; Szenknect, S.; Costin, D. T.; Mesbah, A.; Poinssot, C.; Dacheux, N. From thorite to coffinite: A spectroscopic study of $Th_{1-x}U_xSiO_4$ solid solutions. *Spectrochim. Acta, Part A* **2014**, *118*, 302−307.

(10) Costin, D. T.; Mesbah, A.; Clavier, N.; Szenknect, S.; Dacheux, N.; Poinssot, C.; Ravaux, J.; Brau, H. P. Preparation and characterization of synthetic $Th_{0.5}U_{0.5}SiO_4$ uranothorite. *Prog. Nucl. Energy* **2012**, *57*, 155−160.

(11) Costin, D. T.; Mesbah, A.; Clavier, N.; Dacheux, N.; Poinssot, C.; Szenknect, S.; Ravaux, J. How To Explain the Difficulties in the Coffinite Synthesis from the Study of Uranothorite? *Inorg. Chem.* **2011**, *50* (21), 11117−11126.

(12) Labs, S.; Hennig, C.; Weiss, S.; Curtius, H.; Zanker, H.; Bosbach, D. Synthesis of Coffinite, $USiO_4$, and Structural Investigations of $U_xTh_{(1-x)}SiO_4$ Solid Solutions. *Environ. Sci. Technol.* **2014**, *48* (1), 854−860.

(13) Boatner, L. A. In *Phosphates: Geochemical, Geobiological, and Materials Importance*; Kohn, M. J., Rakovan, J., Hughes, J. M., Ed.; Mineralogical Soc America: WA, 2002; Vol. *48*, pp 87−121.

(14) Ni, Y. X.; Hughes, J. M.; Mariano, A. N. Crystal-chemistry of the monazite and xenotime structures. *Am. Mineral.* **1995**, *80* (1−2), 21−26.

(15) Forster, H. J. The chemical composition of REE-Y-Th-U-rich accessory minerals in peraluminous granites of the Erzgebirge-Fichtelgebirge region, Germany. Part II: Xenotime. *Am. Mineral.* **1998**, *83* (11−12), 1302−1315.

(16) Rapp, R. P.; Watson, E. B. Monazite solubility and dissolution kinetics - implications for the thorium and light rare-earth chemistry of felsic magmas. *Contrib. Mineral. Petrol.* **1986**, *94* (3), 304−316.

(17) Bowring, S. A.; Housh, T. The earth early evolution. *Science* **1995**, *269* (5230), 1535−1540.

(18) Forster, H. J. Composition and origin of intermediate solid solutions in the system thorite-xenotime-zircon-coffinite. *Lithos* **2006**, *88* (1−4), 35−55.

(19) Bea, F. Residence of REE, Y, Th and U in granites and crustal protoliths; Implications for the chemistry of crustal melts (vol 37, pg 521, 1996). *J. Petrol.* **1996**, *37* (6), 1601−1601.

(20) Franz, G.; Andrehs, G.; Rhede, D. Crystal chemistry of monazite and xenotime from Saxothuringian-Moldanubian metapelites, NE Bavaria, Germany. *Eur. J. Mineral.* **1996**, *8* (5), 1097−1118.

(21) Heinrich, W.; Rehs, G.; Franz, G. Monazite-xenotime miscibility gap thermometry 0.1. An empirical calibration. *J. Metamorph. Geol.* **1997**, *15* (1), 3−16.

(22) Buick, R.; Brauhart, C. W.; Morant, P.; Thornett, J. R.; Maniw, J. G.; Archibald, N. J.; Doepel, M. G.; Fletcher, I. R.; Pickard, A. L.; Smith, J. B.; Barley, M. E.; McNaughton, N. J.; Groves, D. I. Geochronology and stratigraphic relationships of the Sulphur Springs Group and Strelley Granite: a temporally distinct igneous province in the Archaean Pilbara Craton, Australia. *Precambrian Res.* **2002**, *114* (1−2), 87−120.

(23) Buick, R.; Thornett, J. R.; McNaughton, N. J.; Smith, J. B.; Barley, M. E.; Savage, M. Record of emergent continental-crust similar-to-3.5 billion years ago in the pibara craton of Australia. *Nature* **1995**, *375* (6532), 574−577.

(24) Scharer, U.; Xu, R. H.; Allegre, C. J. U-Pb Geochronology of gangdese (Transhimalaya) plutonism in the Lhasa-Xigaze region, Tibet. *Earth Planet. Sci. Lett.* **1984**, *69* (2), 311−320.

(25) Scharer, U. The effect of initial Th-230 disequilibrium on young U-Pb ages- the makalu case, Himalaya. *Earth Planet. Sci. Lett.* **1984**, *67* (2), 191−204.

(26) Bowring, S. A.; Erwin, D. H.; Jin, Y. G.; Martin, M. W.; Davidek, K.; Wang, W. U/Pb zircon geochronology and tempo of the end-Permian mass extinction. *Science* **1998**, *280* (5366), 1039−1045.

(27) Gibson, G. M.; Ireland, T. R. Granulite formation during continental extention in Fjordland, New-Zealand. *Nature* **1995**, *375* (6531), 479−482.

(28) Seydoux-Guillaume, A. M.; Wirth, R.; Heinrich, W.; Montel, J. M. Experimental determination of Thorium partitioning between monazite and xenotime using analytical electron microscopy and X-ray diffraction Rietveld analysis. *Eur. J. Mineral.* **2002**, *14* (5), 869−878.

(29) Rasmussen, B.; Fletcher, I. R.; Muhling, J. R.; Wilde, S. A. In situ U-Th-Pb geochronology of monazite and xenotime from the Jack Hills belt: Implications for the age of deposition and metamorphism of Hadean zircons. *Precambrian Res.* **2010**, *180* (1−2), 26−46.

(30) Rasmussen, B.; Fletcher, I. R.; Muhling, J. R. In situ U-Pb dating and element mapping of three generations of monazite: Unravelling cryptic tectonothermal events in low-grade terranes. *Geochim. Cosmochim. Acta* **2007**, *71* (3), 670−690.

(31) Montel, J. M.; Kornprobst, J.; Vielzeuf, D. Preservation of old U-Th-Pb ages in shielded monazite: example from the Beni Bousera Hercynian kinzigites (Morocco). *J. Metamorph. Geol.* **2000**, *18* (3), 335−342.

(32) Montel, J. M.; Razafimahatratra, D.; Ralison, B.; De Parseval, P.; Thibault, M.; Randranja, R. Monazite from mountain to ocean: a case study from Trolognaro (Fort-Dauphin), Madagascar. *Eur. J. Mineral.* **2011**, *23* (5), 745−757.

(33) Andrehs, G.; Heinrich, W. Experimental determination of REE distributions between monazite and xenotime: potential for temperature-calibrated geochronology. *Chem. Geol.* **1998**, *149* (1−2), 83−96.

(34) Dacheux, N.; Clavier, N.; Podor, R. Monazite as a promising long-term radioactive waste matrix: Benefits of high-structural flexibility and chemical durability. *Am. Mineral.* **2013**, *98* (5−6), 833−847.

(35) Schlenz, H.; Heuser, J.; Neumann, A.; Schmitz, S.; Bosbach, D. Monazite as a suitable actinide waste form. *Z. Kristallogr. - Cryst. Mater.* **2013**, *228* (3), 113−123.

(36) Boatner, L.; Sales, B. In *Radioactive Waste Forms for the Future*; Lutze, W., Ewing, R. C., Eds.; 1988; pp 495−564.




DOI: 10.1021/acs.inorgchem.6b01862
*Inorg. Chem.* 2016, 55, 11273−11282

(37) Terra, O.; Dacheux, N.; Audubert, F.; Podor, R. Immobilization of tetravalent actinides in phosphate ceramics. *J. Nucl. Mater.* **2006**, *352* (1), 224−232.
(38) Bregiroux, D.; Terra, O.; Audubert, F.; Dacheux, N.; Serin, V.; Podor, R.; Bernache-Assollant, D. Solid-state synthesis of monazite-type compounds containing tetravalent elements. *Inorg. Chem.* **2007**, *46* (24), 10372−10382.
(39) Terra, O.; Dacheux, N.; Clavier, N.; Podor, R.; Audubert, F. Preparation of optimized uranium and thorium bearing brabantite or monazite/brabantite solid solutions. *J. Am. Ceram. Soc.* **2008**, *91* (11), 3673−3682.
(40) Oelkers, E. H.; Montel, J. M. Phosphates and nuclear waste storage. *Elements* **2008**, *4* (2), 113−116.
(41) Burakov, B. E.; Yagovkina, M. A.; Garbuzov, V. M.; Kitsay, A. A.; Zirlin, V. A. In *Scientific Basis for Nuclear Waste Management XXVIII*; Hanchar, J. M., StroesGascoyne, S., Browning, L., Eds.; 2004; Vol. *824*, pp 219−224.
(42) Ewing, R. C.; Lutze, W.; Weber, W. J. Zircon - a Host-Phase for the Disposal of Weapons Plutonium. *J. Mater. Res.* **1995**, *10* (2), 243−246.
(43) Burghartz, M.; Matzke, H.; Leger, C.; Vambenepe, G.; Rome, M. Inert matrices for the transmutation of actinides: fabrication, thermal properties and radiation stability of ceramic materials. *J. Alloys Compd.* **1998**, *271*, 544−548.
(44) Foerster, H.-J. The chemical composition of REE-Y-Th-U-rich accessory minerals in peraluminous granites of the Erzgebirge-Fichtelgebirge region, Germany; Part I, The monazite-(Ce)-brabantite solid solution series. *Am. Mineral.* **1998**, *83* (3−4), 259−272.
(45) Podor, R.; Cuney, M.; Nguyen, T. C. Experimental study of the solid solution between monazite-(La) and $(Ca_{0.5}U_{0.5})PO_4$ at 780 degrees C and 200 MPa. *Am. Mineral.* **1995**, *80* (11−12), 1261−1268.
(46) Forster, H. J.; Harlov, D. E. Monazite-(Ce)-huttonite solid solutions in granulite-facies metabasites from the Ivrea-Verbano Zone, Italy. *Mineral. Mag.* **1999**, *63* (4), 587−594.
(47) Peiffert, C.; Cuney, M. Hydrothermal synthesis of the complete solid solution between monazite ($LaPO_4$) and huttonite ($ThSiO_4$) at 780 degrees C and 200 MPa. *J. Conf. Abs.* **1999**, *4*, 522.
(48) McCarthy, G. J.; White, W. B.; Pfoertsch, D. E. Synthesis of nuclear waste monazites, ideal actinide hosts for geologic disposal. *Mater. Res. Bull.* **1978**, *13* (11), 1239−1245.
(49) Harlov, D. E.; Wirth, R. Experimental incorporation of Th into xenotime at middle to lower crustal P-T utilizing alkali-bearing fluids. *Am. Mineral.* **2012**, *97* (4), 641−652.
(50) Hanchar, J. M.; Finch, R. J.; Hoskin, P. W. O.; Watson, E. B.; Cherniak, D. J.; Mariano, A. N. Rare earth elements in synthetic zircon: Part 1. Synthesis, and rare earth element and phosphorus doping. *Am. Mineral.* **2001**, *86* (5−6), 667−680.
(51) Ledergerber, G.; Degueldre, C.; Heimgartner, P.; Pouchon, M. A.; Kasemeyer, U. Inert matrix fuel for the utilisation of plutonium. *Prog. Nucl. Energy* **2001**, *38* (3−4), 301−308.
(52) Recktenwald, G.; Deinert, M. Effect of Burnable Absorbers on Inert Matrix Fuel Performance and Transuranic Burnup in a Low Power Density Light-Water Reactor. *Energies* **2013**, *6* (4), 2291−2304.
(53) Dacheux, N.; Brandel, V.; Genet, M.; Bak, K.; Berthier, C. Solid solutions of uranium and thorium phosphates: Synthesis, characterization and X-ray photoelectron spectroscopy. *New J. Chem.* **1996**, *20* (3), 301−310.
(54) Frondel, C.; Collette, R. L. Hydrothermal Synthesis of Zircon, Thorite and Huttonite. *Am. Mineral.* **1957**, *42* (11−2), 759−765.
(55) Frontera, C.; Rodriguez-Carvajal, J. FullProf as a new tool for flipping ratio analysis. *Phys. B* **2003**, *335* (1−4), 219−222.
(56) Ravel, B.; Newville, M. ATHENA, ARTEMIS, HEPHAESTUS: data analysis for X-ray absorption spectroscopy using IFEFFIT. *J. Synchrotron Radiat.* **2005**, *12* (4), 537−541.
(57) Ankudinov, A. L.; Ravel, B.; Rehr, J. J.; Conradson, S. D. Real-space multiple-scattering calculation and interpretation of x-ray-absorption near-edge structure. *Phys. Rev. B: Condens. Matter Mater. Phys.* **1998**, *58* (12), 7565−7576.
(58) Terra, O.; Clavier, N.; Dacheux, N.; Podor, R. Preparation and characterization of lanthanum-gadolinium monazites as ceramics for radioactive waste storage. *New J. Chem.* **2003**, *27* (6), 957−967.
(59) Mesbah, A.; Szenknect, S.; Clavier, N.; Lozano-Rodriguez, J.; Poinssot, C.; Den Auwer, C.; Ewing, R. C.; Dacheux, N. Coffinite, $USiO_4$, Is Abundant in Nature: So Why Is It So Difficult To Synthesize? *Inorg. Chem.* **2015**, *54* (14), 6687−6696.
(60) Taylor, M.; Ewing, R. C. Crystal-structures of $ThSiO_4$ polymorphs, thorite and huttonite. *Trans. Am. Geophys. Union.* **1975**, *56* (12), 1076−1076.
(61) Milligan, W. O.; Mullica, D. F.; Beall, G. W.; Boatner, L. A. Structures of $ErPO_4$, $TmPO_4$, and $YbPO_4$. *Acta Crystallogr., Sect. C: Cryst. Struct. Commun.* **1983**, *39* (1), 23−24.
(62) Martins, J. L.; Zunger, A. Bond lengths around isovalent impurities and in semiconductor solid solutions. *Phys. Rev. B: Condens. Matter Mater. Phys.* **1984**, *30* (10), 6217−6220.
(63) Boyce, J. B.; Mikkelsen, J. C. Local structure of ionic solid solutions: Extended x-ray-absorption fine-structure study. *Phys. Rev. B: Condens. Matter Mater. Phys.* **1985**, *31* (10), 6903−6905.
(64) Mikkelsen, J. C.; Boyce, J. B. Extended x-ray-absorption fine-structure study of $Ga_{1-x}In_xAs$ random solid solutions. *Phys. Rev. B: Condens. Matter Mater. Phys.* **1983**, *28* (12), 7130−7140.
(65) Nästren, C.; Jardin, R.; Somers, J.; Walter, M.; Brendebach, B. Actinide incorporation in a zirconia based pyrochlore $(Nd_{1.8}An_{0.2})$-$Zr_2O_{7+x}$ (An = Th, U, Np, Pu, Am). *J. Solid State Chem.* **2009**, *182* (1), 1−7.
(66) Walter, M.; Somers, J.; Bouëxière, D.; Rothe, J. Local structure in solid solutions of stabilised zirconia with actinide dioxides ($UO_2$, $NpO_2$). *J. Solid State Chem.* **2011**, *184* (4), 911−914.
(67) Begun, G. M.; Beall, G. W.; Boatner, L. A.; Gregor, W. J. Raman-Spectra of the Rare-Earth Ortho-Phosphates. *J. Raman Spectrosc.* **1981**, *11* (4), 273−278.
(68) Syme, R. W. G.; Lockwood, D. J.; Kerr, H. J. Raman-Spectrum of Synthetic Zircon ($ZrSiO_4$) and Thorite ($ThSiO_4$). *J. Phys. C: Solid State Phys.* **1977**, *10* (8), 1335−1348.
(69) Kolesov, B. A.; Geiger, C. A.; Armbruster, T. The dynamic properties of zircon studied by single-crystal X-ray diffraction and Raman spectroscopy. *Eur. J. Mineral.* **2001**, *13* (5), 939−948.
(70) Poloznikova, M. E.; Fomichev, V. V. Vibrational-Spectra and Structure Peculiarities of the I-III Groups Elements Orthophosphates. *Usp. Khim.* **1994**, *63* (5), 419−430.
(71) Strohhofer, C.; Fick, J.; Vasconcelos, H. C.; Almeida, R. M. Active optical properties of Er-containing crystallites in sol-gel derived glass films. *J. Non-Cryst. Solids* **1998**, *226* (1−2), 182−191.
(72) Yu, X. C.; Song, F.; Wang, W. T.; Luo, L. J.; Han, L.; Cheng, Z. Z.; Sun, T. Q.; Tian, J. G.; Pun, E. Y. B. Comparison of optical parameters and luminescence between $Er^{3+}/Yb^{3+}$ codoped phosphate glass ceramics and precursor glasses. *J. Appl. Phys.* **2008**, *104* (11), 113105.
(73) Hoskin, P. W. O.; Rodgers, K. A. Raman spectral shift in the isomorphous series $(Zr_{1-x}Hf_x)SiO_4$. *Eur. J. Solid State Inorg. Chem.* **1996**, *33* (11), 1111−1121.
(74) Geisler, T.; Burakov, B. E.; Zirlin, V.; Nikolaeva, L.; Poml, P. A Raman spectroscopic study of high-uranium zircon from the Chernobyl "lava". *Eur. Eur. J. Mineral.* **2005**, *17* (6), 883−894.


DOI: 10.1021/acs.inorgchem.6b01862
*Inorg. Chem.* 2016, 55, 11273−11282